PCCP

Trapping Ca+ inside a Molecular Cavity: Computational study of the potential energy surfaces for Ca+-[n]cycloparaphenylene, n=5-12

Journal:	*Physical Chemistry Chemical Physics*
Manuscript ID	CP-ART-02-2022-000717.R1
Article Type:	Paper
Date Submitted by the Author:	05-Apr-2022
Complete List of Authors:	Allen, Cole; The University of Texas at Austin, Department of Biomedical Engineering Rempe, Susan; Sandia National Laboratories, Computational Bioscience Zwier, Timothy; Purdue University Ren, Pengyu; University of Texas at Austin, Department of Biomedical Engineering

Trapping Ca^+ inside a Molecular Cavity: Computational study of the potential energy surfaces for Ca^+-[*n*]cycloparaphenylene, *n*=5-12

Cole D. Allen, † Susan L.B. Rempe, ‡* Timothy S. Zwier§* and Pengyu Ren, †*

†Department of Biomedical Engineering, University of Texas at Austin, Austin, TX 78712 USA

‡Center for Integrated Nanotechnologies, Sandia National Laboratories, Albuquerque, New Mexico 87185, USA

§Sandia National Laboratories, Gas Phase Chemical Physics, Livermore, CA 94550 USA

*Susan B. Rempe, Timothy S. Zwier, Pengyu Ren

Email: slrempe@sandia.gov, tszwier@sandia.gov, pren@utexas.edu

Abstract

Ion trap quantum computing utilizes electronic states of atomic ions such as Ca^+ to encode information on to a qubit. To explore the fundamental properties of Ca^+ inside molecular cavities, we describe here a computational study of Ca^+ bound inside neutral [*n*]-cycloparaphenylenes (*n*=5-12), often referred to as “nanohoops”. This *ab initio* study characterizes optimized structures, harmonic vibrational frequencies, potential energy surfaces, and ion molecular orbital distortion as functions of increasing nanohoop size. The results of this work provide a first step in guiding experimental studies of the spectroscopy of these ion-molecular cavity complexes.

I. Introduction

Quantum computing using linear arrays of laser-cooled atomic ions has progressed rapidly from first implementation of quantum logic gates (1, 2) to a relatively mature technology capable of out-performing classical computers on certain types of problems. Trapped atomic ions offer exquisite control over laser cooling, state preparation, entanglement, and read-out.(3) A defining starting point for current ion trap quantum computing is that each atomic ion serves as a single qubit.(3) Atomic ions with single valence-shell electrons (e.g., Ca^+, Yb^+, Ba^+) have simple energy level structures with transitions for cooling and qubit state preparation at wavelengths where compact, high-resolution lasers operate effectively. In Ca^+, the $4^2S_{1/2}$-$4^2P_{1/2}$ transition at 397 nm is used to laser cool the Ca^+ inside the ion trap into a linear array with inter-ion spacing determined by the balance between Coulomb repulsion and the electrostatic trapping potential. The quadrupole-allowed $4^2S_{1/2}$-$3^2D_{5/2}$ transition at 729 nm serves as the atomic qubit, with a spontaneous emission lifetime of ~1 sec. Individual qubits are entangled by state-dependent coupling to the vibrational motions of the ions in the trap, while read-out of the states of the individual qubits occurs via fluorescence.(4, 5)

Molecular ions offer a tantalizing prospect for moving beyond the one qubit per ion limit (6). A common-sense strategy for moving in this direction is in chemically-bound diatomic ions, with their simple vibration-rotation energy level structure.(7-10) However,

the chemical bond drastically alters the electronic structure of the individual atoms, necessitating reconsideration of all aspects of their optical control.(7-10)

This manuscript constitutes a first step in exploring an alternative strategy for incorporating molecular degrees of freedom into ion trap quantum computing and sensing; namely, to bind the same atomic ions used for quantum computing (e.g., Ca^+) inside neutral molecules that serve as a molecular cavity for the ion. The cavitands of interest here are the cycloparaphenylenes, [*n*]CPP, with *n*=5-12, of which *n*=8 is shown below.

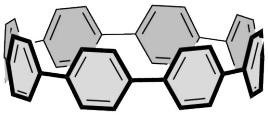

[8]CPP

Cycloparaphenylenes are cyclic macrocycles composed entirely of phenyl rings linked to one another by C-C single bonds. The phenyl rings are oriented nominally perpendicular to the plane of the nanohoop, thereby bearing a structural resemblance to a single belt of an armchair carbon nanotube. These fascinating structures were first synthesized with *n*=9, 12, and 18 phenyl rings by Jasti et al.(11) Since then, a full complement of [*n*]CPP nanohoops have been made that extend from *n*=5-33.(12)

Once the cavity is large enough to accommodate them, ions preferentially bind to the interior of the nanohoops where they interact with the p clouds of more than one phenyl ring.(13) The Ca^+-[*n*]CPP complexes will have molecular energy levels that are sensitive to the size, shape, and mode of binding to the [*n*]CPP binding partner. In the context of quantum computing, it is important to determine if these Ca^+-[*n*]CPP complexes also retain the essential exceptional electronic properties of the Ca^+ that make it the ion of choice for quantum computing. The varying size of the molecular cavity will lead to resolvable, electronic-state dependent vibrational and rotational “fine structure” that will appear in the electronic spectrum of the Ca^+-[*n*]CPP complex.

Beyond its potential application as an active component or sensor in quantum computing, the properties and spectroscopy of metal ion-[*n*]CPP complexes are interesting in their own right. The binding of alkali metal ions to benzene is a prototypical

ion-ligand interaction, with a preferred binding site along the 6-fold axis of benzene and an experimental $K^+\cdots$benzene binding energy of 17.5 kcal/mol.(14) Analogous experimental studies of the binding energies of bare metal ions to [*n*]CPP are not yet available; however, one anticipates that the interaction will be strongest on the interior of the molecular cavity where contributions to the binding energy from more than one phenyl ring are possible. Calculations of doubly reduced [*n*]CPP^{-2} (*n*= 6, 8, 10, and 12) bound with multiple alkali metals have been studied by Zhou et al. (15) Ueno et al.(16) recently synthesized and characterized the nested binding of Li^+@C60 inside [10]CPP, while Rogachev et al.(17) studied the $[K^+(THF)_2]_4$[8]CPP salt in which K^+ ions are bound both on the interior and exterior of four-fold reduced [8]CPP^{-4} anion. To our knowledge, there have been no studies of neutral CPP and Ca^+ ion complexes.

In the computational study reported here, we focus attention on the ground electronic state properties of a series of Ca^+-nanohoop complexes, calculating optimized ground state structures, harmonic vibrational frequencies, and binding energies for the Ca^+-[*n*]CPP complexes as a function of nanohoop size for *n*=5-12. We also map out the potential energy surfaces as a function of the Ca^+ location inside the molecular cavities. As we shall see, the Ca^+ ion is predicted to bind to a localized binding pocket along the axis of one of the phenyl rings, creating an annular trough inside the hoop, with small barriers between adjacent sites. The nanohoops deform to accommodate the Ca^+ binding.

II. Computational Details and Methods

To validate the quantum mechanical (QM) methods and density functional theory (DFT) functionals used, a test case on a well-documented model system was undertaken using Gaussian16 software (18). The model system chosen was the ion complex formed between a singly-charged ion and neutral benzene (M^+-benzene). We focused on Ca^+, due to its relevance to this project, and the alkali metal ions Na^+ and K^+ that are similar in size to Ca^+. We explored a range of computational methods using the modest-sized 6-31+g(d) basis set for computational efficiency. The functionals tested were selected based on our previous experience with the functionals B3LYP (19, 20),

B3LYP-GD3BJ (21), and wB97X-D (22) applied to alkylbenzenes (23). Single-point calculations were carried out over a range of distances between cation and the center of benzene. The results are presented as the basis set superposition error (BSSE)(24)-corrected association energy of the complex as a function of distance between the benzene molecule and the ion.

Not surprisingly, there is little previous work on Ca^+ as a binding partner due to its uncommon charge state. Calcium ion exists in most circumstances as Ca^{2+}, thus most studies focus on the divalent calcium ions (25). There are several previous studies of alkali metal ions interacting with benzene, as they form a prototypical system that is sensitive to polarization and dispersion of the benzene p electron cloud (26-28). In particular, a recent study by Savarese et al. compared a range of computational methods and dispersion corrections on Li^+-benzene complexes and showed that for some methods, such as DFT B3LYP, the inclusion of an empirical dispersion correction resulted in qualitative and quantitative differences from the reference CCSD(T) complete basis set (CBS) (29) limit (30). This result prompted us to study the M^+-benzene (Bz) complex using computational methods capable of being extended to the large nanohoop cavities.

DFT B3LYP calculations were carried out at the 6-31+G(d) level of theory with, and without, Grimme's D3(BJ) dispersion correction, and at the wB97X-D level of theory which includes Grimme's D2 dispersion correction. The results from these two methods were compared with those from the symmetry-adapted perturbation theory (SAPT) (31) energy decomposition method using the PSI4 software package (32). SAPT decomposes the interaction energies into electrostatics, exchange, induction, and dispersion components. Many levels of SAPT can be used. In this work the highest level of SAPT available for a given system was chosen. For the Ca+ system, SAPT0 was chosen. SAPT0 utilizes first-order classical electrostatic, and second-order electrostatic induction, dispersion, and correction terms. For K+ and Na+ systems, SAPT2+ was chosen. SAPT2+ incorporates intramolecular correlational effects in the dispersion term (33). SAPT0 was chosen for the Ca+ systems because only SAPT0 is available for open-shelled systems in PSI4, whereas higher versions of SAPT are available for closed-shelled systems. It should be noted that SAPT for open-shelled systems is less

studied and the accuracy is not well established relative to close-shelled SAPT (34). For Ca+-benzene, we further performed CCSD(T)/CBS (MP2/def2-[T/Q]ZVPD with CCSD(T)/def2-[D/T]ZVPD) single point calculations to evaluate the binding energy. The benzene was optimized on its own using wB97X-D/6-31+G(d) and the resulting structure was used in all benzene-ion calculations. The ions were placed at different distances from the center-of-mass of the benzene ring along the six-fold axis of the benzene. The BSSE corrected association energy of the M^+-Bz complex was calculated as a function of distance between benzene and the ion.

For K^+-Bz and Na^+-Bz, the highest level SAPT energy decomposition, SAPT2+, was used as the benchmark. The results for Na^+-Bz and K^+-Bz are shown in **Figures 1** and **2**, respectively. Both complexes show similar trends for the DFT methods studied. The B3LYP calculations without dispersion correction and wB97X-D both have smooth curves with shapes similar to SAPT0 and SAPT2+ references, and errors in energy under ~1.5 kcal/mol. We further performed SAPT2+ calculations using the aug-cc-pVTZ basis set to examine the convergence of SAPT2+ with basis set size. The larger basis set SAPT2+ results, especially around the minimum, moved lower and become more similar to SAPT0. However, the potential energy curves calculated with B3LYP-GD3(BJ) have a qualitatively different shape from the SAPT2+ results. In the Na^+-Bz complex, the GD3(BJ) correction produces a substantially wider well in the potential energy surface than the other methods, while in the K^+-Bz complex, this same correction leads to a double minimum in the potential energy curve. The location of the global minimum in the potential energy surface is also ~0.5 Å greater with the B3LYP-GD3(BJ) approach than all other methods.

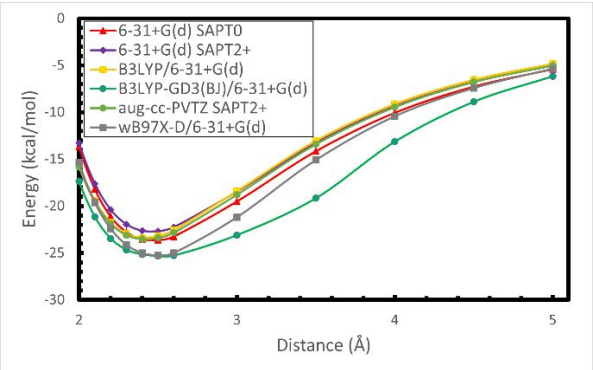

Figure 1: Calculated Na^+-Bz potential

energy curve for motion of Na^+ along the 6-fold axis of benzene (through the center and perpendicular to the benzene plane). SAPT0 and SAPT2+ results are used as the refences for comparison with B3LYP, B3LYP-GD3(BJ) and wB97X-D DFT methods. All calculations employed the 6-31+G(d) basis set.

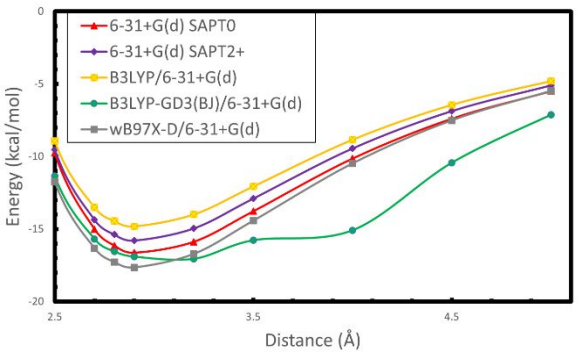

Figure 2: Calculated K^+-Bz potential energy curve for motion of K^+ along the 6-fold axis of benzene. SAPT0 and SAPT2+ calculations are used as the references for comparison with B3LYP, B3LYP-GD3(BJ) and wB97X-D DFT methods. All calculations employed the 6-31+G(d) basis set.

The corresponding results for Ca^+-Bz in **Figure 3** show that the B3LYP-GD3(BJ) energy curve differs significantly from the SAPT0 and other DFT results, with its minimum at a substantially further Ca^+-Bz distance. Once again, the B3LYP functional without the dispersion correction provides a better qualitative and quantitative match with SAPT0 results than B3LYP when the dispersion correction is added. Despite this agreement, wB97X-D is the best overall match with SAPT0 for the Ca^+-Bz system, both quantitatively and qualitatively. Since the main focus of this study is the Ca^+-[*n*]CPP (*n*=5-12) complexes, all calculations were carried out using the wB97X-D/6-31+G(d) level of theory in the remainder of this work.

In addition to the SAPT0 results, CCSD(T)/CBS calculations were conducted for selected points around the minima. CCSD(T)/CBS is considered the 'gold standard' in quantum mechanics calculations (35). The CCSD(T)/CBS results on the absolute binding energy shifted even lower; however, the trend including the location of energy minima, is similar to the SAPT0 as well as wB87X-D results.. It is computationally prohibitive to perform CCSD(T)/CBS calculations for the entire surfaces of the larger CPPs. Thus, the computationally tractable DFT method wB97X-D was selected based on the comparisons made so far. We acknowledge the limitation of the DFT results for the magnitude of binding energy, and in this study we focus on the shape and relative trend of the energy landscapes.

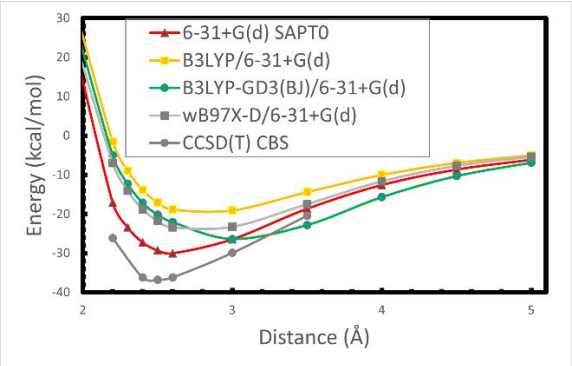

Figure 3: Calculated Ca^+-Bz potential energy curve for motion of Ca^+ along the 6-fold axis of benzene. SAPT0

calculations are used as the references for comparison with B3LYP, B3LYP-GD3(BJ) and wB97X-D DFT methods. All calculations employed the 6-31+G(d) basis set. CCSD(T)/CBS calculations for select points around minima are also included.

The optimized structures for each of the Ca^+-[*n*]CPP complexes with *n*=5-12 were found by first optimizing the [*n*]CPP nanohoop in the absence of the Ca^+. Using this nanohoop geometry as the starting structure, next the complex structure was optimized, with the Ca^+ placed at the center-of-mass of the nanohoop. Harmonic vibrational frequency calculations of the [*n*]CPP complexes at the optimized geometry showed no imaginary frequencies, indicating that the optimized geometries were actual minima (36).

Rigid potential energy surfaces (PES) were calculated by placing the Ca^+ ion at different positions in the central horizontal plane (x,y) across the nanohoop within a rigid nanohoop **(Figure 4)**. The nanohoop is held fixed at its optimized geometry in the absence of the Ca^+, thereby allowing no distortion of the nanohoop in response to the Ca^+. We varied the Ca^+ position over a symmetric slice of the interior space of each nanohoop in a series of single point calculations. The grid of points used to locate the Ca^+ was defined using the distance of the ion from the center of mass (*r*) of the nanohoop and an angle (*q*) that varied from q to q + (360/n) where “n” is the number of phenyl rings in [n]CPP. Only $1/n^{th}$ of the nanohoop was sampled due to the approximate *n*-fold symmetry of the nanohoop. The sampled “slice” covered one phenyl ring and one bond between phenyl rings. The resulting rigid slice is dependent on the orientation of the phenyl rings because the nanohoop was not allowed to change geometry in response to the Ca^+. These results provide an initial estimate of the PES. The polar coordinates were converted to Cartesian coordinates in the PES plots. The PESs were plotted using MATLAB 2021.

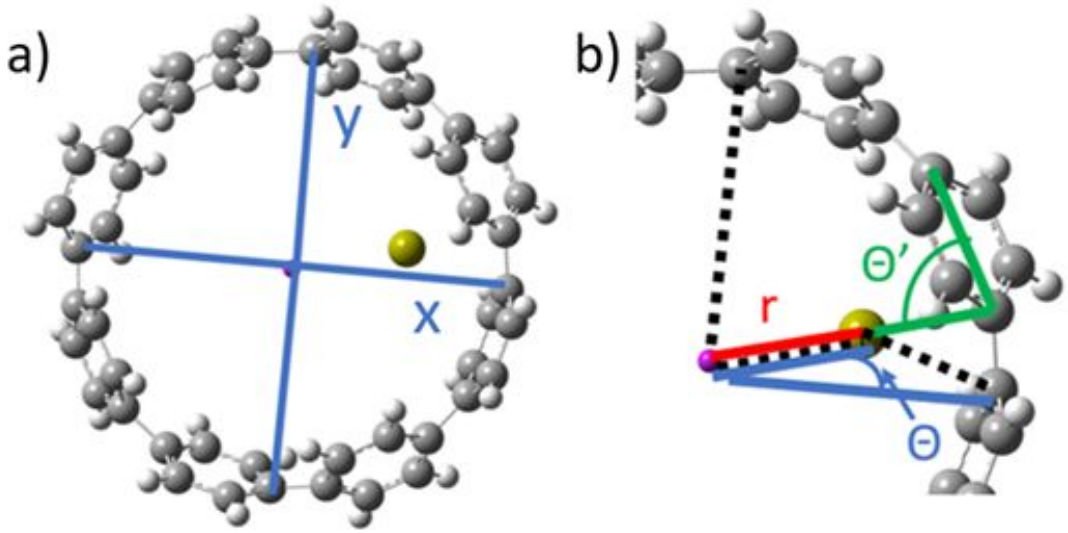

Figure 4: Coordinates used for PES mapping. A) Linear angles used to fix the dummy atom in the center of the nanohoop (origin). These axes are also used to define the x and y axes of the Cartesian coordinate system. B) Radius *r* (red) and angle *Θ* (blue) of a polar coordinate system for locating the ion, with origin at the dummy atom. *Θ* (blue) has its zero along the x axis. *Θ'* (green) is defined as the angle between the ion and two coplanar carbons on the same phenyl ring. It was used as the angular restraint in the relaxed PES scans, while the actual polar angle is *Θ* (blue). The dashed line (black) shows the dihedral between C(i)-dummy-ion-C(f).

Relaxed PES scans were performed by using the rigid PES inputs as starting structures and optimizing them while imposing constraints to keep the ion fixed to a series of polar coordinates, with more points being added around the minima. The restraints are shown in **Figure 4**. This strategy allowed for distortion of the nanohoop in response to the Ca^+ position, unlike in the rigid PES. A dummy atom was placed at the nanohoop center of mass and used as the origin for imposing constraints, which included two linear angles, a distance, a nonlinear angle, and a dihedral angle. The two linear angle constraints (a special angle restraint for angles close to 180°) used two coplanar carbon atoms on opposite sides of the nanohoop and the dummy atom to fix the dummy atom in place. The distance restraint fixed the distance *r* between the

dummy atom and the ion. The nonlinear angle specified an angle between two coplanar carbons on the same phenyl ring and the ion. This angle was chosen to aid calculations with the ion closer to the nanohoop. The actual polar angle Θ was measured between ion-dummy-carbon, as shown in **Figure 4(b)**. The dihedral angle restraint (black dashed lines) used two coplanar carbons, the dummy atom and the ion to ensure that the ion remained in the horizontal (x,y) plane of the nanohoop. The resulting relaxed slice of the potential energy surface is independent of the orientation of the phenyl rings because we are mapping out the surface in the (x,y) plane, and the nanohoop was allowed to change geometry in response to the Ca^+. This procedure ensured *n*-fold symmetry to the PES and the need for calculation of only one relaxed PES slice. The coordinates were converted to Cartesian and plotted in MATLAB, just as in the rigid PES scan.

III. Results and Discussion

A. Optimized Structures and Binding Energies

The optimized geometries for the Ca^+-[*n*]CPP complexes with *n*=5-12 are shown in **Figure 5**. The striking result is that, at the wB97X-D/6-31+G(d) level of theory, none of the complexes have a minimum with Ca^+ at the center of the nanohoop, but instead prefer the ion in an off-center geometry. Notably, throughout the series, the distance between the ion and the nearest phenyl ring in the optimized structure approaches that taken by the Ca^+ in the Ca^+-Bz complex (2.60 Å). Furthermore, the ion sits near the center of a phenyl ring face rather than atop the C-C bond linking the adjacent phenyl rings. The exception to this rule is in *n*=5, which is unusual in many respects, as it represents the smallest stable [*n*]CPP nanohoop and presents a binding pocket nearly the size of Ca^+ itself. In the optimized structures, the *n*=5 nanohoop distorts around the ion significantly as the ion approaches the nanohoop, maximizing the Ca^+ interaction with two phenyl rings. Such distortion is not observed in the larger nanohoops as it is energetically unfavorable.

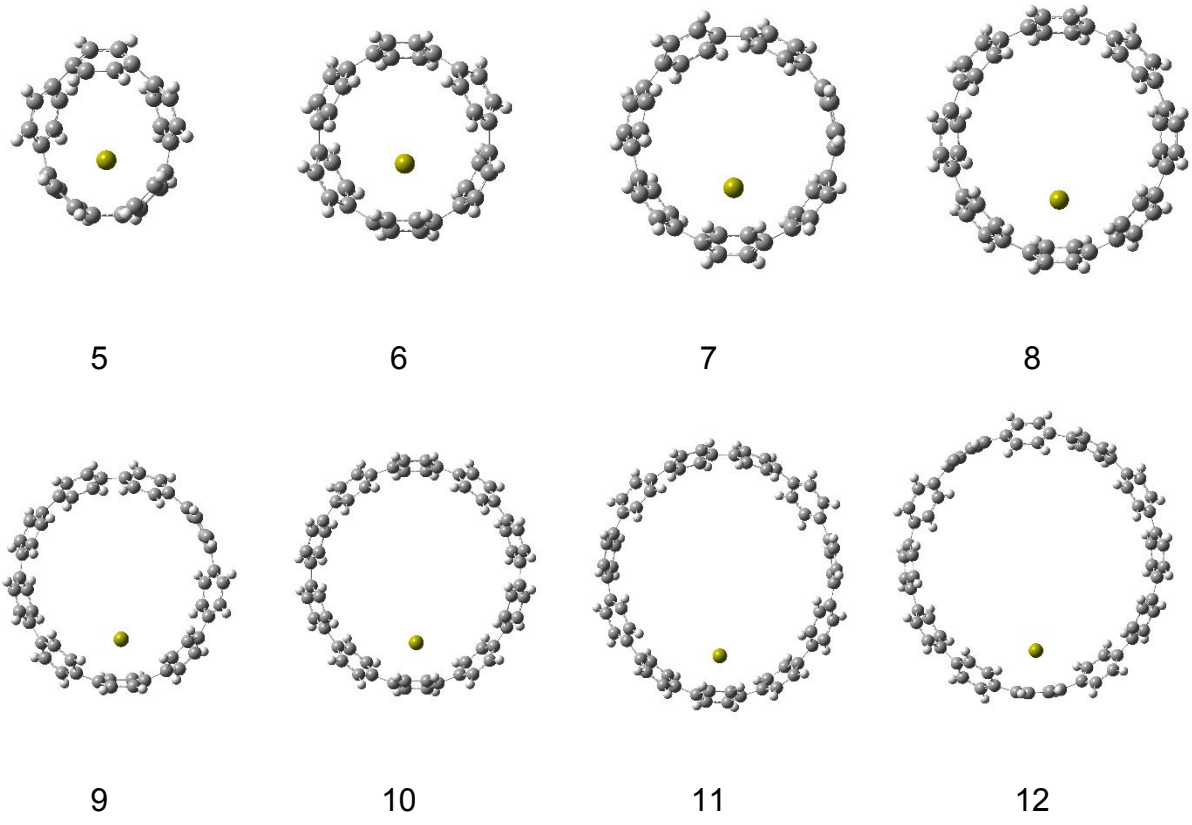

Figure 5: Optimized structres for Ca^+-[*n*]CPP (*n*=5-12) complexes using wB97X-D/6-31+G(d) level of theory. The numeric label for the nanohoop size (beneath the structure) denotes the number of phenyl rings that make up the nanohoop.

Table 1: Basis set superposition error (BSSE) and zero-point energy (ZPE) corrected association energies, binding energies, and transition barrier energies for each Ca^+-[*n*]CPP (*n*=5-12) complex calculated at the wB97X-D/6-31+G(d) level of theory.

[*n*]CPP	Ion-Nanohoop Distance (Å)[5]	ΔE_{ZPE}[1] (kcal/ mol)	ΔE_{BSSE} (kcal/ mol)	E_{TS}[2] (kcal/ mol)	ΔE_{Asso}[3] (kcal/ mol)	ΔE_{Bind}[4] (kcal/ mol)
[5]CPP	2.40	-0.90	1.46	1.82	-67.52	-56.79
[6]CPP	2.77	0.55	1.05	0.06	-40.61	-39.33
[7]CPP	2.65	0.75	1.00	1.41	-38.45	-36.97

[8]CPP	2.63	0.69	0.93	0.49	-37.27	-35.89
[9]CPP	2.62	0.63	0.85	n/a	-36.58	-35.26
[10]CPP	2.62	0.71	0.85	n/a	-35.88	-34.60
[11]CPP	2.62	0.62	0.82	n/a	-35.49	-34.29
[12]CPP	2.61	0.68	0.79	n/a	-35.30	-34.25
[5]CPP flat	2.67	0.79	0.79	n/a	-31.89	-31.26
[3]CPP flat	2.69	0.80	0.75	n/a	-30.33	-29.82
Ca^+-Bz	2.6	0.75	0.36	n/a	-22.68	-22.25
Ca^+-[8]CPP Outside	2.78	0.63	0.87	n/a	-32.75	-32.00

[1] $\Delta E_{ZPE} = ZPE_{complex} - ZPE_{CPP}$
[2] $E_{TS} = E_{max} - E_{min}$; Values extracted from the minimum energy path (**Figure 9**)
[3] $\Delta E_{Asso} = E_{complex} - E_{Apo\,CPP} - E_{Apo\,Ca^+} + \Delta E_{ZPE} + \Delta E_{BSSE}$, where Apo is defined as nanohoop geometry fixed to its geometry in the complex.
[4] $\Delta E_{Bind} = E_{complex} - E_{Opt\,CPP} - E_{Opt\,Ca^+} + \Delta E_{ZPE} + \Delta E_{BSSE}$
[5] Distance from the Ca^+ to the center of the nearest phenyl ring.

Table 2: Atomic Mulliken charges for Ca^+ ion in the Ca^+-[*n*]CPP complex as a function of nanohoop size.

[*n*]CPP	q_{Ca^+}(e)
[5]CPP	1.30
[6]CPP	0.52
[7]CPP	0.66
[8]CPP	0.71
[9]CPP	0.74
[10]CPP	0.75
[11]CPP	0.75
[12]CPP	0.75

The binding energies of the series of complexes are summarized in **Table 1**. Correction for zero-point energy and basis-set superposition error, used in obtaining the best estimate binding energies, are shown in the far-right column of the table. Here we define the binding energy as the difference between the complex energy and the sum of the two monomers (nanohoop as one and ion as the other), optimized individually. We define the association energy as the difference between the complex energy and the sum of the two monomers held as they are in the complex.

In general, the binding and association energies decrease as the nanohoop size increases, dropping from -56.8 kcal/mol in *n*=5 to an asymptote of about -34.2 kcal/mol in *n*=11 and 12. The difference between the binding energy and association energy for each complex gets smaller as the nanohoop size increases, indicating that the distortion of the nanohoop induced by the ion decreases as the nanohoop gets larger.

To test this notion, we calculated binding and association energies for a "flat" Ca^+-[5]CPP analog, which consisted of 5 phenyl rings in a linear chain (C_6H_5-$(C_6H_4)_3$-C_6H_5) that is placed flat to simulate an infinitely large nanohoop. A "flat [3]CPP" binding partner for Ca^+ was also studied to isolate the contribution of the two adjacent phenyl rings to the binding energy. The difference in binding energy for the "flat [3]CPP" and "flat [5]CPP" complexes is small (~ 5% of the total BE), indicating that the majority of the binding of Ca^+ to [*n*]CPP occurs through the closest phenyl ring and the two adjacent phenyl rings on either side.

Note that the asymptotic binding energy for Ca^+ to the *n*=11 and 12 (34.5 kcal/mol) nanohoops is about 10% greater than that to Ca^+-"flat"-[5]CPP (-31.3 kcal/mol), indicating that the accumulated stabilization of the ion complex from interaction with other phenyl rings more remote in the nanohoop is small, but not entirely negligible. By contrast, the smallest nanohoops with *n*=5 and 6 have substantially larger binding energies than the larger nanohoops, indicating that Ca^+ gains further stabilization when the nanohoop size is a good fit with the ion size, with near-optimal distances for ion binding with all phenyl groups in the nanohoop.

The majority of the binding in these complexes is due to ion-induced dipole interactions between the ion and phenyl ring π (pi) clouds. However, charge transfer

between the ion and nanohoop π clouds also plays a role. While the assignment of charge between the ion and nanohoop is ill-defined, we report in **Table 2** the Mulliken charges of the Ca^+ in the optimized structures. The Ca^+ atomic charges asymptotically approach +0.75 as the nanohoop size increases due to the ion being further away from the π clouds of the adjacent phenyl rings on the nanohoop. Once again, [5]CPP acts as an outlier due to the Ca^+ interacting with more phenyl rings due to the small size of the nanohoop.

B. Vibrational Analysis and Inter-Ring Barriers

Harmonic vibrational frequencies were calculated for all members of the series and are reported in the Supplementary Material. Ca^+-[8]CPP is used here as a representative complex since the vibrational modes with significant Ca^+ motion remain remarkably similar with varying nanohoop size. The displacement vectors associated with the three harmonic frequency vibrational normal modes corresponding to ion motion are shown in **Figure 6a-c**, respectively, while their vibrational frequencies are listed in **Table 3**. These vibrational modes are associated with movement of the ion (a) tangentially along a direction toward adjacent phenyl rings, (b) radially in the nanohoop, and (c) in and out of the nanohoop cavity. The motions of the nanohoop relative to the Ca^+ aren't simple counter-displacements, as the low-frequency motions of the nanohoop themselves mix to some degree with the pseudo-translational motions of the ion. The frequencies for the vibrational modes generally decrease as nanohoop size increases, indicating a softening of the potential around the minimum energy point(s) on the surface. This reflects the decrease in total binding energy with nanohoop size.

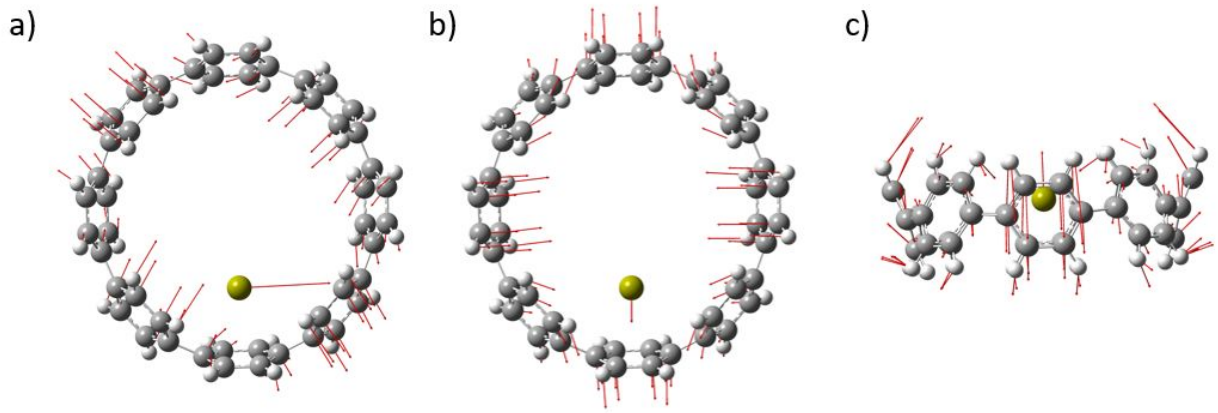

Figure 6: The optimized structure for Ca^+-[8]CPP with displacement vectors for normal (harmonic) vibrational modes corresponding to ion movement at the wB97X-D/6-31+G(d) level of theory. The displacement vectors are shown for a) tangential, b) radial, and c) in/out of plane movement of the ion.

Table 3: Three harmonic vibrational mode frequencies (cm^{-1}) corresponding to ion movement in each Ca^+-[*n*]CPP (*n*=5-12). Normal mode displacements are shown in **Figure 6**.

[*n*]CPP	[5]CPP	[6]CPP	[7]CPP	[8]CPP	[9]CPP	[10]CPP	[11]CPP	[12]CPP
Tangential	28.40	19.16	20.29	19.64	15.27	13.23	11.57	8.64
Radial	56.19	35.20	29.24	23.54	18.09	14.99	12.60	10.55
In/Out of Plane	94.21	46.16	67.49	38.73	42.29	40.37	37.96	39.08

C. Potential Energy Surfaces for Ca^+ motion inside the nanohoop

Initial attempts to approximate the potential energy surface (PES) for Ca^+ ion motion inside the nanohoops proceeded with the nanohoop geometry held fixed at its optimized geometry and the Ca^+ placed at the center of the nanohoop. These "rigid" PES slices are included Supplementary Material for *n*=5, 6, and 8. However, the inherent flexibility of the nanohoop is significant, enabling it to respond to the location of the Ca^+ through reorientation of the phenyl rings and distortion of the nanohoop away from a circular orientation. We focus attention on nanohoops with *n*=5-8 as the larger nanohoops with *n*=9-12 are similar in shape to those of *n*=8.

Two different views of the relaxed PES for the Ca^+-[8]CPP complex are shown in **Figure 7**. On the left, a 45^o slice of the PES for Ca^+ motion is shown, which subtends a single phenyl ring and the C-C bond joining this ring to its neighbor. On the right, this 45^o slice is replicated eight times to show the entire 360^o interior space of the nanohoop. **Figure 8** presents the full interior PES for each of the nanohoops with *n*=5-8. The qualitative features include a peak at the center, an annular valley closer to the nanohoop, and a repulsive wall at larger *r* as the ion approaches the nanohoop wall. This gives the PES's a sombrero shape. [8]CPP is representative of larger nanohoops as their qualitative features are very similar. For the smallest nanohoop (*n*=5), we show only the central "crown", since optimizations close in to the nanohoop wall failed to converge. The height of the barrier (a second-order transition state) at the center of the nanohoop varies non-monotonically with nanohoop size, with smallest barrier of only 0.06 kcal/mol in *n*=6. As Figure 8 shows, the potential energy surface for n=6 is nearly flat for Ca^+ motion over the entire 3.14 $Å^2$ interior area of the nanohoop.

The relaxed PESs generally showed very little variation in energy for annular motion at fixed radial position *r* of the Ca^+. Indeed, at the optimized distance *r*, the barrier for ion movement along the annular trough tangential to the nanohoop walls is only about 0.5 kcal/mol (175 cm^{-1}), and varies only slightly with nanohoop size. Since the tangential vibrational mode (Figure 6a) that moves along this annular trough has a frequency less than 30 cm^{-1}, the zero-point energy is well below the barrier, and the Ca^+ should possess an 'n'-fold degenerate zero-point level with localization above a single phenyl ring. For instance, in a cryo-cooled ion trap on the one hand, the population resides primarily in the vibrational zero-point level (T_{vib}~10 K).(37) On the other hand, at

room temperature where kT (energy) = 0.6 kcal/mol, Ca^+ would have sufficient average energy to move along this annular trough. Furthermore, this modest barrier should lead to highly anharmonic vibrational mode structure within a couple of hundred wavenumbers of the zero-point level, leading to fascinating spectroscopy if the vibrational transitions can be resolved.

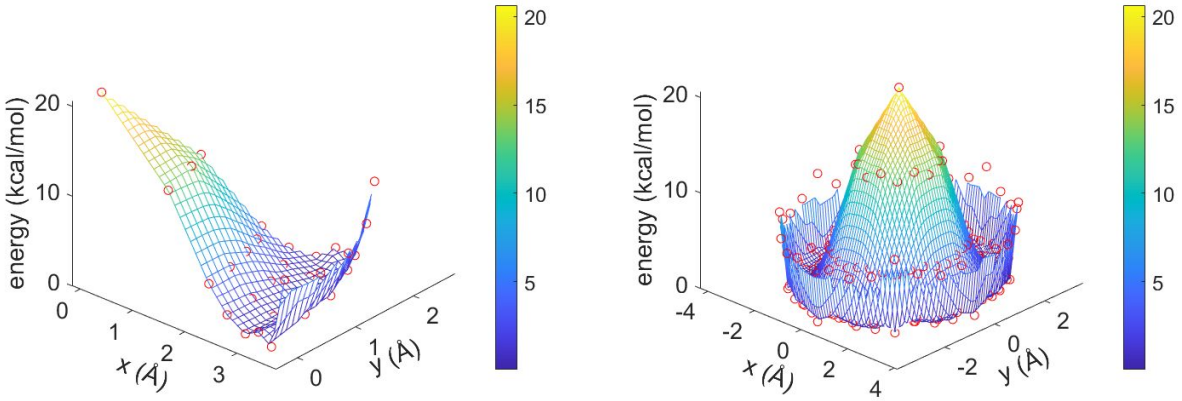

Figure 7: Relaxed potential energy surface for a 45 degree slice of the Ca^+-[8]CPP complex (left) and the full 360° surface (right) using wB97X-D/6-31+G(d). Each red circle represents a location at which the ion was fixed. All energy values are relative to the global minimum.

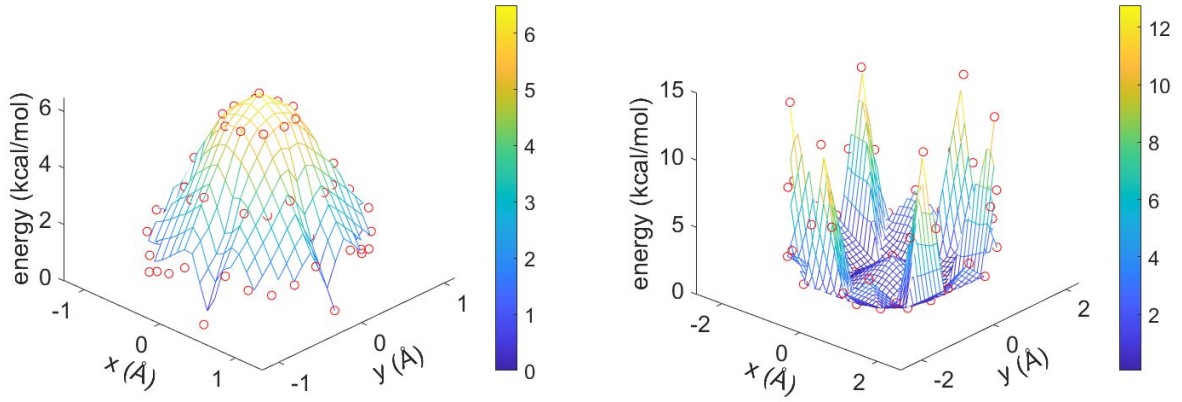

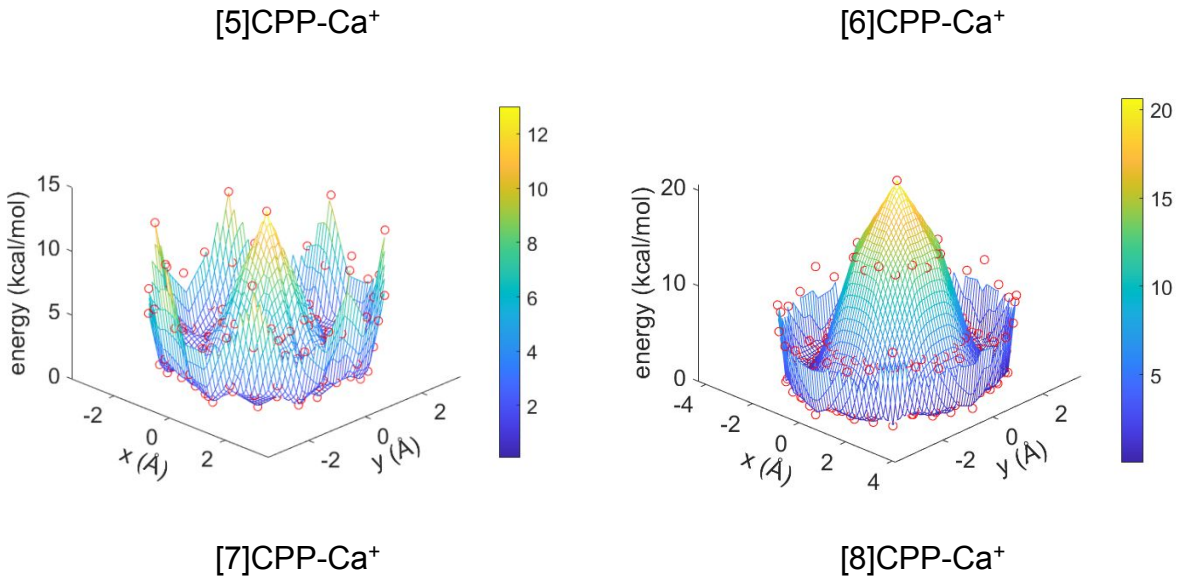

Figure 8: Full relaxed potential energy surfaces for Ca^+-[*n*]CPP (*n*=5-8) complexes using wB97X-D/6-31+G(d). Each red circle represents a location at which the ion was fixed. All energy values are relative to the global minimum. For the Ca^+-[5]CPP complex convergence difficulties prevented getting close enough to the nanohoop to see the outer wall.

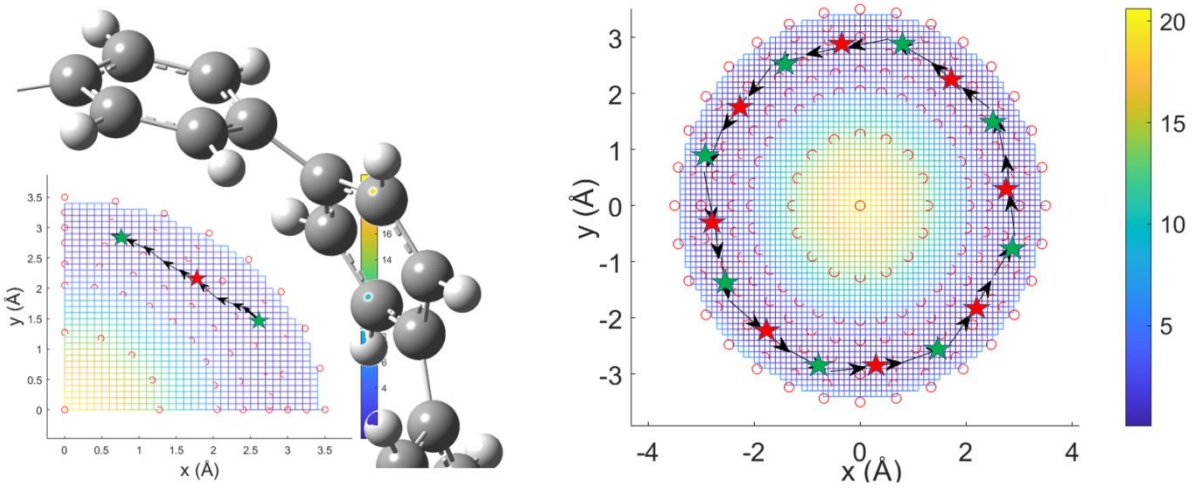

Figure 9: The minimum energy pathway between two adjacent minima (left) and full nanohoop (right) in Ca^+-[8]CPP complex . The minima are denoted with green stars. The transition states to annular motion between minima are denoted with red stars. The

barrier sits above the C-C bond between phenyl rings, which act as a good approximation of actual saddle points.

Using an interpolated form of the relaxed potential energy surface for the Ca^+-[8]CPP complex, a minimum energy pathway for motion between successive phenyl rings was mapped out (**Figure 9**, left) and then combined to show the pathway for full motion along the nanohoop annulus (right). As anticipated, the corrugation in the surface with annular motion is quite small, with an over-all pathway that is nearly circular, but pushes away from the wall by about 0.15 Å as it passes over the C-C bond joining adjacent phenyl rings.

Finally, optimization of Ca^+ bound to the exterior of [8]CPP shows it to have a binding energy of -32.00 kcal/mol (**Table 1**), just 4 kcal/mol less favorable than its interior binding energy. By extrapolation, we surmise that there is a second annular trough for Ca^+ motion outside of the nanohoop. Note that while binding to the interior of the nanohoop is always preferred, the energy difference between the internal and external annular troughs decreases as the nanohoop size increases. Finally, while we have not explored directly the potential energy surface for Ca^+ motion between the interior and exterior of the nanohoop cavity, even the weakest binding position inside the nanohoop, at its center-point, is anticipated to be well below the barrier for motion around the walls of the nanohoop from interior to exterior.

D. Influence of nanohoop on the Ca^+ ground electronic state

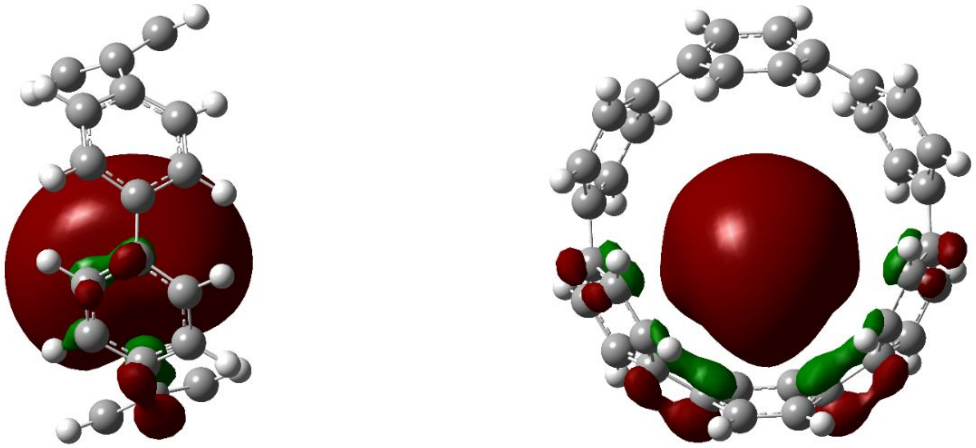

[6]CPP SOMO

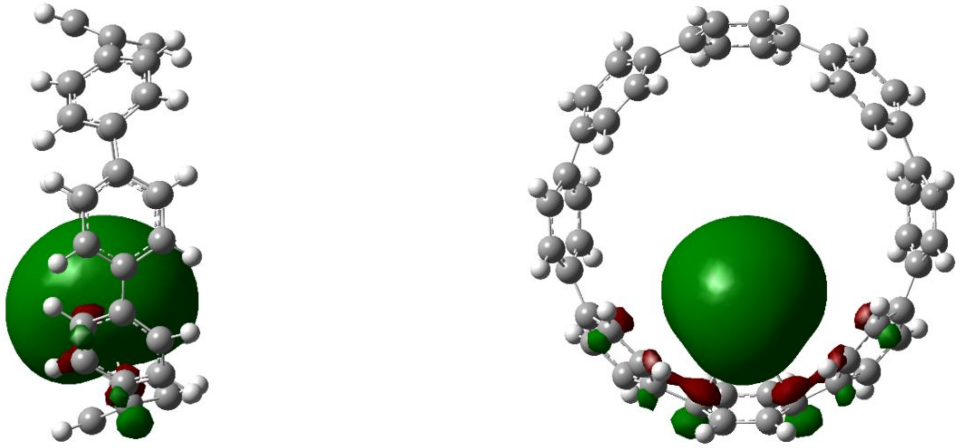

[8]CPP SOMO

Figure 10: Singly occupied molecular orbitals for Ca^+-[6]CPP and Ca^+-[8]CPP complexes. Side (left) and frontal (right) views are shown to describe the distorted s orbital of the Ca^+.

A primary motivation for this work is to predict the ground electronic state properties of the Ca^+-[*n*]CPP complexes as starting points for electronic spectroscopy that explores the electronic transitions of Ca^+ inside this molecular cavity. Recall that the

ground electronic configuration of atomic Ca^+ is $[Ar]4s^1$. When placed inside a perfectly spherical molecular cavity, by symmetry the "s" orbital would retain its shape, similar to how the Ca^+ would experience a spherically symmetric binding potential. However, in the nanohoops, the phenyl rings present a "belt" of high electron density that will distort the 4s orbital away from spherical symmetry.

To visualize these distortions, **Figure 10** presents the singly occupied molecular orbitals (SOMO) for [6]CPP and [8]CPP as representative cases. As anticipated, in both sized nanohoops, the HOMO is a distorted atomic-like orbital on the Ca^+ in which the electron density is polarized away from the nanohoop wall to which it is binding most strongly. The shape of the distorted 4s orbital is similar for Ca^+-[*n*]CPP for *n*=6-12.

By contrast, Ca^+ fits tightly within the nanohoop interior of Ca^+-[5]CPP, the smallest and most strained nanohoop. The ion's electron density occupies a large fraction of the available space, which leads to a unique and difficult-to-describe distortion to the 4s orbital (see Supplementary Material, **Figure S3**). This tight fit leads to much stronger binding than other members of the series (**Table 1**). We see once again that [5]CPP is an outlier relative to *n*=6-12, and surmise on this basis that [5]CPP is a less optimal candidate for spectroscopic exploration than the larger nanohoops, particularly *n*=6, with its nearly flat-bottomed potential for Ca+ motion.

IV. Conclusions

We report computational predictions of the optimized structures, binding energies, harmonic vibrational frequencies and potential energy surfaces for Ca^+ motion in the series of Ca^+-[*n*]CPP complexes with *n*=5-12. In all cases but n=5, the Ca^+ prefers to bind atop one of the phenyl rings, away from the nanohoop center, gaining additional favorable interactions from the adjacent phenyl rings on either side. The binding energy of Ca^+ inside the nanohoop generally decreases as the nanohoop size grows, varying from 56 kcal/mol in Ca^+-[5]CPP to 34 kcal/mol in *n*=11 and 12. This binding energy for Ca^+ is only about 5% larger than that for Ca^+-"flat [5]CPP" complex that simulates an infinitely large nanohoop, but about 9 kcal/mol greater than in the Ca^+-benzene complex.

The potential energy surface for Ca^+ ion motion inside the nanohoop has a nearly circular trough with a minimum at about 2.60 Å from the nanohoop wall. Small barriers to motion between phenyl rings asymptotically approach ~0.5 kcal/mol with increasing nanohoop size. Thus, Ca^+ is free to move nearly freely along this annulus, although the zero-point levels show significant localization above individual phenyl rings. Notably, there is a second annular trough about equidistance outside the nanohoop, which is only ~ 4 kcal/mol less strongly bound for n=8. The energy peak at the nanohoop center varies non-monotonically with nanohoop size, with a lowest value of ~2.5 kcal/mol in n=6. Mulliken charges place much of the positive charge on the Ca^+ in the complex, but also point to some degree of sharing of the positive charge with the nanohoop. Finally, the singly-occupied molecular orbital (SOMO) for $n \geq 6$ is a distorted 4s orbital localized on the Ca^+ where the single unpaired electron resides. This result indicates that, at least in the electronic ground state, Ca^+ retains much of its electronic character, as it must if these complexes are to be useful in ion trap quantum computing.

Conflicts of interest

There are no conflicts of interest to declare.

Acknowledgements

This work was supported by the Laboratory Directed Research and Development program at Sandia National Laboratories, a multi-mission laboratory managed and operated by National Technology and Engineering Solutions of Sandia LLC, a wholly owned subsidiary of Honeywell International Inc. for the U.S. Department of Energy's National Nuclear Security Administration under contract DE-NA0003525. CA and PR acknowledge support for this work from a Sandia Academic Alliance Grant 21-0149 (contract agreement number 1885207). Calculations were performed, in part, at the Center for Integrated Nanotechnologies, an Office of Science User Facility operated for the U.S. Department of Energy (DOE) Office of Science. The views expressed in the article do not necessarily represent the views of the U.S. DOE or the United States Government.

Supplementary Material

The supplementary material includes raw QM data for Na^+-Bz, K^+-Bz, and Ca^+-Bz calculations, raw QM data for binding energy, association energy, ZPE and BSSE correction, plotted PES data, raw QM data for PES, rigid and relaxed PESs not shown in main text, molecular orbital figures for [5]CPP, and a link to the input/output files on GitHub.

References

1. Benhelm J, Kirchmair G, Roos CF, Blatt R. Towards fault-tolerant quantum computing with trapped ions. Nature Physics. 2008;4(6):463-6.
2. Cirac JI, Zoller P. QUANTUM COMPUTATIONS WITH COLD TRAPPED IONS. Physical Review Letters. 1995;74(20):4091-4.
3. Brown KR, Kim J, Monroe C. Co-designing a scalable quantum computer with trapped atomic ions. Nature Partner Journals Quantum Information. 2016;2.
4. Brown KR, Kim J, Monroe C. Co-designing a scalable quantum computer with trapped atomic ions. Npj Quantum Information. 2016;2:16034.
5. Werth G, Gheorghe VN, G MF. Quantum Computing with Trapped Charged Particles. Charged Particle Traps II: Springer Series on Atomic, Optical and Plasma Physics; 2009. p. 207-56.
6. Calvin AT, Brown KR. Spectroscopy of Molecular Ions in Coulomb Crystals. Journal of Physical Chemistry Letters. 2018;9(19):5797-804.
7. Calvin AT, Janardan S, Condoluci J, Rugango R, Pretzsch E, Shu G, et al. Rovibronic Spectroscopy of Sympathetically Cooled (CaH+)-Ca-40. Journal of Physical Chemistry A. 2018;122(12):3177-81.
8. Hudson ER, Campbell WC. Dipolar quantum logic for freely rotating trapped molecular ions. Physical Review A. 2018;98(4).
9. Staanum PF, Hojbjerre K, Skyt PS, Hansen AK, Drewsen M. Rotational laser cooling of vibrationally and translationally cold molecular ions. Nature Physics. 2010;6(4):271-4.
10. Wolf F, Wan Y, Heip JC, Gebert F, Shi CY, Schmidt PO. Non-destructive state detection for quantum logic spectroscopy of molecular ions. Nature. 2016;530(7591):457-+.
11. Jasti R, Bhattacharjee J, Neaton JB, Bertozzi CR. Synthesis, Characterization, and Theory of 9 -, 12 -, and 18 Cycloparaphenylene: Carbon Nanohoop Structures. Journal of the American Chemical Society. 2008;130(52):17646-+.
12. Leonhardt EJ, Jasti R. Emerging applications of carbon nanohoops. Nature Reviews Chemistry. 2019;3(12):672-86.
13. Della Sala P, Talotta C, Caruso T, De Rosa M, Soriente A, Neri P, et al. Tuning Cycloparaphenylene Host Properties by Chemical Modification. Journal of Organic Chemistry. 2017;82(18):9885-9.
14. Amicangelo JC, Armentrout PB. Absolute binding energies of alkali-metal cation complexes with benzene determined by threshold collision-induced dissociation experiments and ab initio theory. Journal of Physical Chemistry A. 2000;104(48):11420-32.
15. Zhou Z, Wei Z, Schaub TA, Jasti R, Petrukhina MA. Structural deformation and host-guest properties of doubly-reduced cycloparaphenylenes, [Chem Sci. 2020;11(35):9395-401.
16. Ueno H, Nishihara T, Segawa Y, Itami K. Cycloparaphenylene-Based Ionic Donor-Acceptor Supramolecule: Isolation and Characterization of Li+@C-60 subset of 10 CPP. Angewandte Chemie-International Edition. 2015;54(12):3707-11.

17. Rogachev AY, Zhou Z, Liu SY, Wei Z, Schaub TA, Jasti R, et al. Stretching 8 cycloparaphenylene with encapsulated potassium cations: structural and theoretical insights into core perturbation upon four-fold reduction and complexation. Chemical Science. 2021;12(19):6526-35.
18. Frisch MJ, Trucks GW, Schlegel HB, Scuseria GE, Robb MA, Cheeseman JR, et al. Gaussian 16 Rev. C.01. Wallingford, CT2016.
19. Becke AD. Density-functional thermochemistry. III. The role of exact exchange. J Chem Phys. 1993;98:5648-52.
20. Lee C, Yang W, Parr RG. Development of the Colle-Salvetti correlation-energy formula into a functional of the electron density. Phys Rev B Condens Matter. 1988;37(2):785-9.
21. Grimme S, Ehrlich S, Goerigk L. Effect of the damping function in dispersion corrected density functional theory. J Comput Chem. 2011;32(7):1456-65.
22. Chai JD, Head-Gordon M. Long-range corrected hybrid density functionals with damped atom-atom dispersion corrections. Phys Chem Chem Phys. 2008;10(44):6615-20.
23. Hewett DM, Bocklitz S, Tabor DP, Sibert Iii EL, Suhm MA, Zwier TS. Identifying the first folded alkylbenzene. Chem Sci. 2017;8(8):5305-18.
24. van Dujineveldt FB, van Dujineveldt-van de Rijdt JGCM, van Lenthe JH. State of the Art in Counterpoise Theory. Chem Rev. 1994;94(7):1973-885.
25. Jiao D, King C, Grossfield A, Darden TA, Ren P. Simulation of Ca2+ and Mg2+ solvation using polarizable atomic multipole potential. J Phys Chem B. 2006;110(37):18553-9.
26. Wójcik P, Korona T, Tomza M. Interactions of benzene, naphthalene, and azulene with alkali-metal and alkaline-earth-metal atoms for ultracold studies. J Chem Phys. 2019;150(23):234106.
27. Ferretti AadIMaPG. Benchmarking Cation–π Interactions: Assessment of Density Functional Theory and Möller–Plesset Second-Order Perturbation Theory Calculations with Optimized Basis Sets (mp2mod) for Complexes of Benzene, Phenol, and Catechol with Na+, K+, Rb+, and Cs+. The Journal of Physical Chemistry A. 2020;124(17):3445-59.
28. Kumar N, Gaur AS, Sastry GN. A perspective on the nature of cation-π interactions. Journal of Chemical Sciences. 2021;133(4):1-13.
29. Perdew JP, Ruzsinszky A, Constantin LA, Sun J, Csonka GI. Some Fundamental Issues in Ground-State Density Functional Theory: A Guide for the Perplexed. J Chem Theory Comput. 2009;5(4):902-8.
30. Savarese M, Bremond E, Adamo C. Exploring the limits of recent exchange-correlation functionals in modeling lithium/benzene interaction. Theor Chem Acc. 2016;135(4):99-109.
31. Jeziorski B, Moszynski R, Szalewicz K. Perturbation Theory Approach to Intermolecular Potential Energy Surfaces of van der Waals Complexes. Chemical Reviews. 1994;94(7):1887-930.
32. Turney JM, Simmonett AC, Parrish RM, Hohenstein EG, Evangelista FA, Fermann JT, et al. Psi4: an open-source ab initio electronic structure program. WIREs Computational Molecular Science. 2012;2(4):556-65.
33. Parker TM, Burns LA, Parrish RM, Ryno AG, Sherrill CD. Levels of symmetry adapted perturbation theory (SAPT). I. Efficiency and performance for interaction energies. J Chem Phys. 2014;140(9).
34. Patkowski K. Recent developments in symmetry-adapted perturbation theory. Wiley Interdisciplinary Reviews: Computational Molecular Science. 2020;10(3):e1452.
35. Raghavachari K, Trucks G, Pople J, Head-Gordon M. A fifth-order perturbation comparison of electron correlation theories. Chemical Physics Letters. 2013;589:37-40.
36. Rempe SB, Jónsson H. A computational exercise illustrating molecular vibrations and normal modes. The Chemical Educator. 1998;3(4):1-17.
37. Harrilal CP, DeBlase AF, Fischer JL, Lawler JT, McLuckey SA, Zwier TS. Infrared Population Transfer Spectroscopy of Cryo-Cooled Ions: Quantitative Tests of the Effects of Collisional Cooling on the Room Temperature Conformer Populations. J Phys Chem A. 2018;122(8):2096-107.